Wang *et al. Green Manuf Open* 2023;1:2
DOI: 10.20517/gmo.2022.03

Green Manufacturing Open

Research Article

Open Access

Forming mechanism and tribological properties of a Ni-based coating prepared from transverse static magnetic field-assisted supersonic plasma spraying

Zhiyuan Wang[1,2], Yanfei Huang[2], Haidou Wang[2,3], Debin Shan[1], Zhiguo Xing[2]

[1]School of Materials Science and Engineering, Harbin Institute of Technology, Harbin 150001, Heilongjiang, China.
[2]National Key Lab for Remanufacturing, Army Academy of Armored Forces, Beijing 100072, China.
[3]National Engineering Research Center for Remanufacturing, Army Armored Forces Institute, Beijing 100072, China.

Correspondence to: Dr. Debin Shan, School of Materials Science and Engineering, Harbin Institute of Technology, 92 Xidazhi Street, Nangang District, Harbin 150001, Heilongjiang, China. E-mail: shandebin@hit.edu.cn; Dr. Zhiguo Xing National Key Lab for Remanufacturing, Army Academy of Armored Forces, 21 Dujiakan, Fengtai District, Beijing 100072, China. E-mail: xingzg2011@163.com

How to cite this article: Wang Z, Huang Y, Wang H, Shan D, Xing Z. Forming mechanism and tribological properties of a Ni-based coating prepared from transverse static magnetic field-assisted supersonic plasma spraying. *Green Manuf Open* 2023;1:2. https://dx.doi.org/10.20517/gmo.2022.03

Received: 30 Jun 2022 **First Decision:** 20 Jul 2022 **Revised:** 21 Jul 2022 **Accepted:** 7 Aug 2022 **Published:** 22 Aug 2022

Academic Editor: Hongchao Zhang **Copy Editor:** Tiantian Shi **Production Editor:** Tiantian Shi

Abstract

Magnetic field-assisted forming represents an environmentally friendly, contactless and high-efficiency technology for the development of advanced *in situ* manufacturing. The application of this technology provides a new concept for improving the properties of ferromagnetic wear-resistant coatings. In this study, we combine magnetic field-assisted forming with supersonic plasma spraying to prepare a Ni-based coating assisted by a transverse static magnetic field. The porosity of the magnetic field-assisted coating is below 2%, the hardness of the coating increases from 638.46 to 785.45 MPa and the tribological coefficient decreases from 0.466 to 0.422. The presence of the static magnetic field directly affects the bubble movement during the forming process of the coating, which makes the bubbles escape outward and reduces the porosity of the coating. The presence of the static magnetic field also further improves the phase structure of the coating, so that the magnetic domain distribution is uniform and the hard phase inside the coating increases. Finally, the residual stress and tribological properties of the coating are also improved.

Keywords: Magnetic field-assisted forming, transverse static magnetic field, supersonic plasma spraying, wear-resistance performance

INTRODUCTION

Remanufacturing represents an energy-saving, green and environmental protection technology. It is also an important direction for advanced manufacturing technology to introduce the high-density energy field into material remanufacturing processes to assist or directly prepare remanufactured products[1-5]. Among them, magnetic field-assisted forming has been widely used for its unique green, contactless, high-efficiency and *in situ* manufacturing characteristics[6-10]. In particular, applying a magnetic field in the process of ferromagnetic metal thermal processing can effectively improve the grain size of the metal, optimize the structure and enhance the material properties. Moreover, magnetic field-assisted molding can produce higher quality equipment parts with the same energy consumption and processing cycle. This, therefore, provides a stable and reliable process for the green molding manufacturing of equipment.

In previous studies, researchers have devoted significant attention to the actual service performance of remanufactured products, particularly the tribological performance. Yin *et al.* analyzed the tribological damage information of engineering products[11]. The authors reported that tribological systems exhibit subject coupling and time and system dependence, which have led to a wide range of data sources and numerous theoretical models in tribological research. The final research objectives are to analyze the mechanisms of the anti-friction and anti-wear mechanisms of the components through the control of the processing technology to make the parts have the effect of abrasion and friction reduction[12].

Qi *et al.* prepared Co-based coatings on a 42CrMo substrate and applied a transverse static magnetic field to analyze the performance changes of the coatings[13]. As the magnetic induction intensity increased, the average grain size in the equiaxed grain region of the top cladding layer decreased from 9.73 to 2.86 μm. The average microhardness reached 1056 HV, representing an improvement of ~23% compared with the non-processed sample. Tharajak *et al.* prepared poly(ether-ether-ketone) (PEEK) composite coatings using a static magnetic field. The tribological properties of the coatings were improved[14]. The specific wear rate decreased by 48% (from 33×10^{-6} to 17×10^{-6} mm^3 Nm^{-1}) for the coating at a 5 N load and by 23% (from 26×10^{-6} to 20×10^{-6} mm^3 Nm^{-1}) for the coating at 25 N. A magnetic field could be used to successfully reduce the friction coefficient and have a positive effect on the wear resistance of PEEK coatings, with a more pronounced effect of the magnetic field being observed when a low applied load of 5 N was used. The PEEK coatings showed different hardnesses and crystallinities in different magnetic field environments, and the most pronounced effect was observed at 100 μm. The results showed that the magnetic field could be applied to the thermal spraying process. Hu *et al.* prepared a NiCrBSi coating by a transverse static magnetic field-assisted laser cladding process and analyzed the molten pool flow of the coating by finite element simulations[15]. The results showed that the electromagnetic force airflow, the convection pool and the acoustic streaming effect changed the macroscopic flow of the melt. Under the action of the magnetic field, the structure of the coating was refined, and the element segregation and mechanical properties were improved.

In summary, magnetic fields have a good effect on the processing and forming of molten metals, especially ferromagnetic metals. Supersonic plasma spraying has always been an important means of protecting the surface of structural parts because of its high temperature and speed[16-18]. It has unique advantages in preparing high melting point metal coatings. It can be found that the flow of molten powder can be improved by using magnetic field auxiliary equipment to strengthen the supersonic plasma spraying

process. This can improve the forming quality of the coating, especially the hardness of the coating and the tribological properties[19]. However, in recent years, due to the complexity of the supersonic plasma spraying process, few studies have directly reported the magnetic field-assisted supersonic plasma spraying process. Therefore, this study focuses on exploring the mechanism of magnetic field assistance in supersonic plasma spraying coating and analyzes the ability of a magnetic field to improve the coating performance of remanufactured parts. Based on the changes in porosity, the magnetic domain, phase transition and mechanical and tribological properties of the Ni-based coating and the mechanism of magnetic domain-assisted thermal spraying are presented.

MATERIALS AND METHODS

Coating preparation

A Ni60 coating was prepared using a transverse static magnetic field-assisted supersonic plasma spraying device, as shown in Figure 1. The structure of the equipment is shown in Figure 1. On the basis of supersonic plasma spraying developed by the State Key Laboratory of Remanufacturing Technology, China, a group of neodymium-iron-boron magnets were added. The position of the two magnets is shown in the figure and a transverse static magnetic field was generated on the surface of the sample. The mean field intensity of the sample surface measured by a gauss meter could reach 0.3 mT. The coating base of the experiment was 1045 steel. The coating powder was Ni60B powder [Ni (bal.), Cr (16.49 wt.%), B (3.53 wt.%), Si (2.17 wt.%) and Fe (15.74 wt.%)]. Other detailed components are shown in Table 1.

The powder shows magnetism and can be attracted by magnets, which is beneficial for exploring the effect of a magnetic field on the spraying mechanism. We prepared two kinds of coatings in a non-magnetic field (referred to as NMF) environment and a magnetic field environment (referred to as MF), respectively. The parameters for the supersonic plasma spraying for both kinds of coatings were the same, namely, a spraying voltage of 115 V, a spraying current of 430 A, a H_2 flow of 17 L/min, an Ar_2 flow of 100 L/min and a spraying distance of 120 mm. The effect of the lateral static magnetic field was analyzed by repeated spraying ten times to form a thick coating. The coating formed after repeated spraying could better show the effect of the magnetic field.

Coating characterization and evaluation

The performance of the above two coatings was tested based on the changes of the coating morphology and mechanical and tribological properties. The morphology of the two coatings was analyzed by scanning electron microscopy (SEM, Supra55, Zeisi, Germany). Simultaneously, the morphology of the coatings was analyzed by energy-dispersive spectroscopy (EDS). The accelerating voltage of the equipment was 10 kV. The section morphology of the coatings and the morphology of the coating wear marks were mainly observed, with the performance change of the coatings analyzed. The magnetic domain distribution was analyzed using atomic force microscopy (AFM, Dimension Icon, Brook, Germany). The device mainly used the interatomic force between the tip of the probe and the sample surface to characterize the surface topography and magnetic properties of the samples. Before the start of the test, the equipment was calibrated with standard samples and the tapping mode was selected for magnetic domain observation. The domain image was then formed by detecting the difference between the phase angle of the voltage drive signal and the vibration phase angle of the microcantilever probe. The phase structure of the coatings was characterized by X-ray diffraction (XRD, D8 Advance, Broker, Germany). The target material of the experiment was a Cr target with a tube current of 6.7 mA and a tube voltage of 30 kV. The test angle range was 0-90°, the spot size was 3 mm and the exposure time was 5 s. The residual stress and hardness of the coatings were mainly tested using an X-ray stress analyzer (XSTRESS Robot, STRESSTECH, Finland). The microhardness of the cross sections of the coatings was measured with a Shimadzu HMV-2000 Vickers hardness tester [Shimadzu Enterprise Management (China) Co., Ltd., Hong Kong, China]. The hardness

Table 1. Compositions of spraying materials

Spraying materials	Elemental content (wt.%)							
	Ni	Fe	Cr	B	Si	C	Mn	S
Ni60B powder	Bal.	15.34	16.49	3.53	2.17			
45# steel substrate		Bal.			0.28–0.48	0.42–0.50	0.51–0.60	0.01–0.069

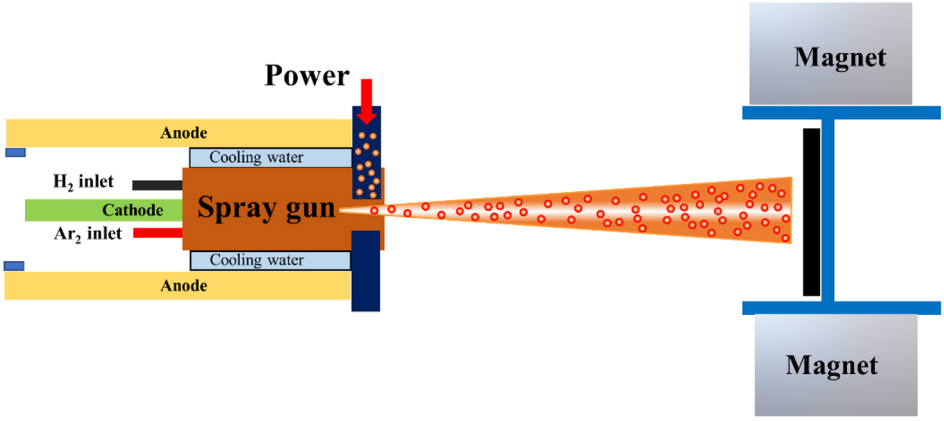

Figure 1. Transverse static magnetic field-assisted supersonic plasma spraying device.

values were measured from the substrate material to the coating surface and the hardness curve was fitted. The tribological performance was tested by a ball-on-disc friction and wear tester (UMT-5 Brucker Corporation, USA). The loading stress of the device was 40 N, the duration was 30 min and the frequency was 10 Hz. The length of the abrasion mark was 5 mm. Finally, a Contour GT-K 3D was used to analyze the morphology of the wear marks.

RESULTS AND DISCUSSION

Morphologic characteristics

SEM morphology of coatings

The cross-sectional morphology of the two coatings is shown in Figure 2, in which Figure 2A shows the NMF coating and Figure 2B presents the MF coating. Six photos of each coating were selected for porosity statistics. As can be seen from Figure 2A, the pore distribution of the NMF coating is random and large pores are the main ones. Furthermore, unmelted particles can be seen in Figure 2A1, A3, A4, A5 and A6, with large pores clustered around the unmelted particles. These directly result in the increase of the porosity of the coating. The porosity statistics are shown in red. It can be seen that the porosity of NMF samples is above 2%. This is the normal range for supersonic plasma spraying. The porosity of the MF samples is below 2%, with the porosity obviously promoted; as can be found in Figure 2B, the coating of the pore is small. In Figure 2B2, B4 and B6, it can be found that there are unmelted particles, but there are no pores around B2 and B4, which is related to the effect of transverse magnetic fields. As the powder is magnetic, it is attracted by the magnetic field when it is spread out, thus increasing the fluidity and rapidly discharging some bubbles. Therefore, the pores of the MF coating are relatively small.

In order to better compare the pore changes of the two coatings, we used industrial CT equipment to slice the coatings and analyze the spatial distribution of the pores and the change of the porosity. Samples of the same size were selected for the pore distribution statistics. Figure 3 shows the 3D pore distribution results of the two coatings. Figure 3A shows the NMF sample and Figure 3B presents the MF sample. Figure 3A1

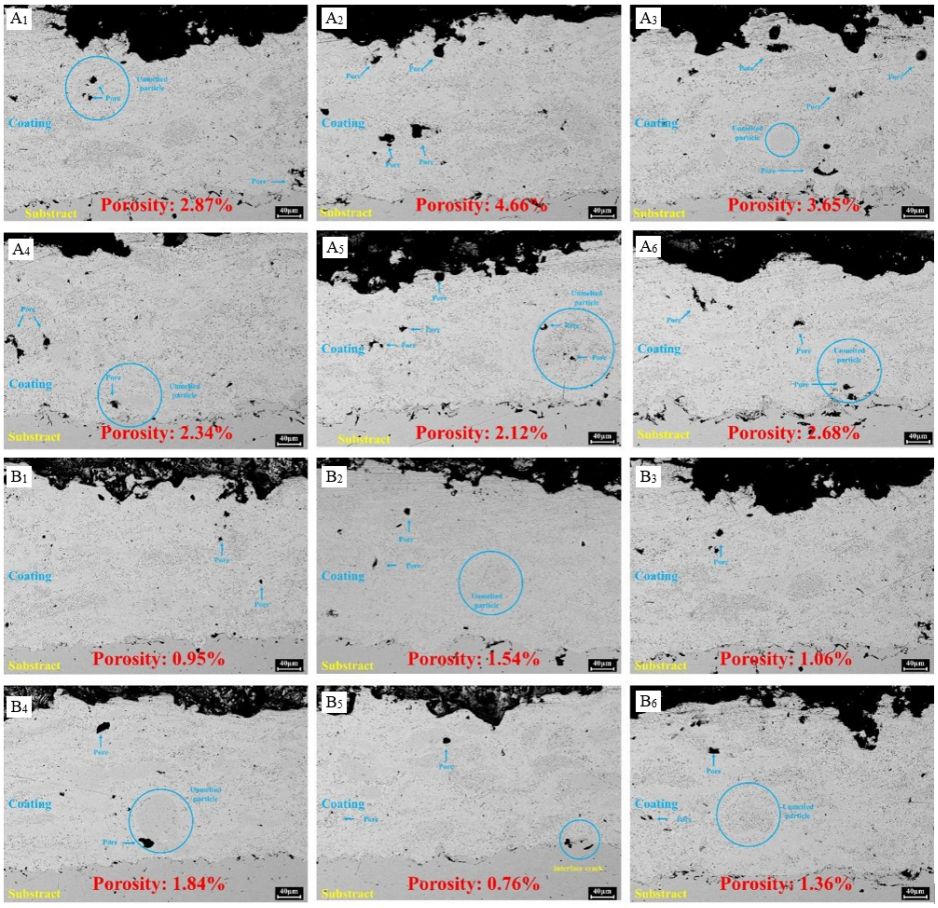

Figure 2. Pore distribution results of coatings: (A) NMF; (B) MF.

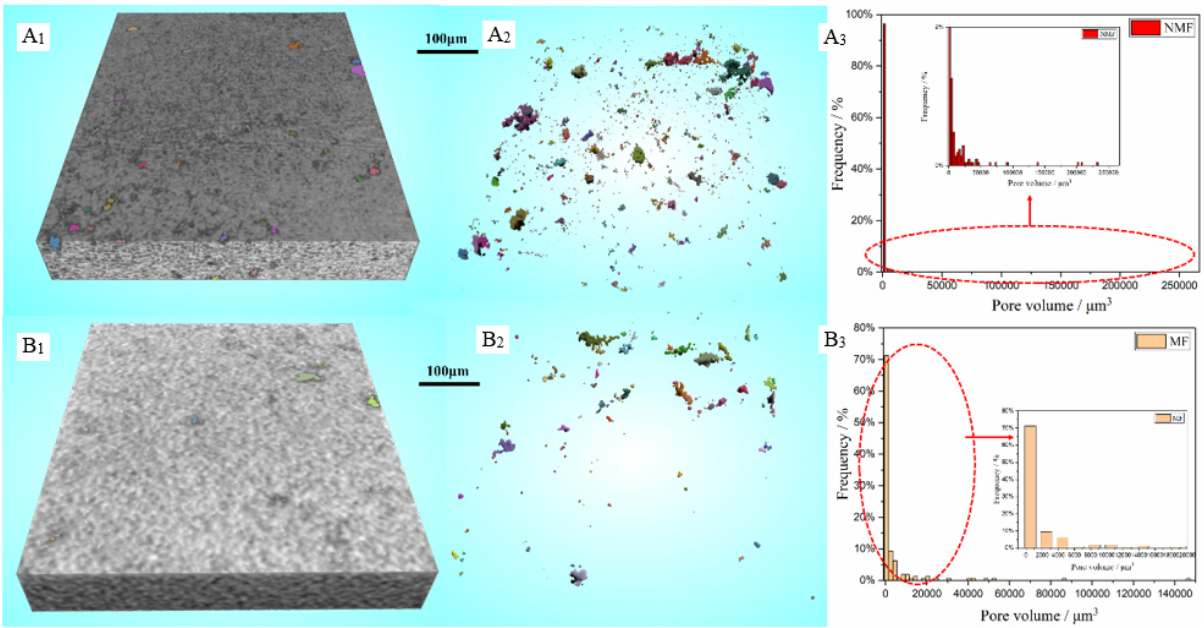

Figure 3. 3D porosity results of coatings. (A_1) NMF sample morphology. (A_2) NMF sample pore morphology. (A_3) NMF sample pore statistical histogram. (B_1) MF sample morphology. (B_2) MF sample pore morphology. (B_3) MF sample pore statistical histogram.

shows the measurement results of the 3D structure, where the actual dimension of the cut coating is: length: 700 μm; width: 550 μm; height: 100 μm. The pore map calculated by the threshold segmentation method is shown in Figure 3A2. The frequency distribution histogram of the pore statistics in the coating is shown in Figure 3A3. The total pore volumes of the two materials are 2122310 and 751712 μm^3, respectively. Therefore, the porosity of the two coatings is 5.512% and 1.952%, respectively. By comparing the 3D porosity results of the two samples, it can be found that the pore size of the MF sample is smaller and the number is less. However, the pores are also concentrated at one end of the coating. This is related to the effect of the transverse magnetic field. The static magnetic field accelerates the fluidity of the molten pool and finally leads to the movement of pores in one direction, and most pores can escape, which improves the porosity of the coating.

Magnetic domain morphology of coatings

The magnetic domain distribution results of the coating are shown in Figure 4. Figure 4A gives the result of the NMF coating and Figure 4C shows the result of the MF coating. By comparison, it can be seen that the magnetic domain distribution of the NMF sample is relatively scattered, while the magnetic domain of the MF shows an obvious strip magnetic domain. This is related to the application of a transverse static magnetic field. Simultaneously, in order to better observe the changes of magnetic domain, we conducted magnetic domain distribution statistics at the horizontal lines in Figure 4A and C. The results are shown in Figure 4B and D. It can be seen that the peaks and troughs of the magnetic domain distribution of the NMF sample are random and have no fixed law. The distribution of MF shows a sinusoidal change. All of these can well prove that the magnetic field distribution of MF sample is more regular. The regular distribution of magnetic domain is related to the internal stress of the coating, which will affect the change of magnetic moment inside the coating and improve the distribution of the magnetic domain[20-22].

Phase structure of coatings

The phase structure changes of the coating were analyzed by XRD, as shown in Figure 5. It can be seen that the diffraction peak height of NMF's main peak is relatively high, indicating that the phase is relatively concentrated. MF is relatively low and its phase content is relatively more. By comparing the PDF cards and automatic peak finding calibration, it can be found that they all contain γ-Ni, BCr, Fe_2Si, Cr_3Si and $FeNi_3$ phases. The main phases γ-Ni, BCr and Cr_7C_3 were calibrated by the crystal orientation index. It can be found by comparing the results that the three phases of $Cr_{23}C_6$, Cr_7C_3 and Cr_3Ni_2Si are special in the MF coating. These are the phases that appear in the coating after the addition of magnetic field. The peak strength of the structure is not high and the content is not stable, but they can be calibrated. This also reflects the effect of the magnetic field. The presence of stable magnetic field improves the coating process and forms a variety of strengthening phases containing Cr to enhance the service performance of the coating.

Forming mechanism of spray coating assisted by transverse static magnetic field

It can be seen from the above that the transverse static magnetic field has a good effect on improving the microstructure, mechanics and tribological properties of the supersonic plasma spray coating. The results show that the porosity and hardness of the MF coating are reduced, the residual stress is compressive stress and its tribological properties are improved. Therefore, we discuss the forming mechanism of the coating and analyze the reasons for its performance improvement. The structural model of the transverse static magnetic field-assisted supersonic plasma spraying coating is shown in Figure 6A. The substrate of the coating is in the middle of two magnetic fields, and the droplets from the spray gun impact the substrate surface at high speed to form the coating. The droplets mostly fly at high temperatures and speeds in the form of spherical particles. They will be spread out after hitting the substrate and finally piled into a coating. However, under the action of transverse static magnetic field, the powder droplet is magnetic and will be

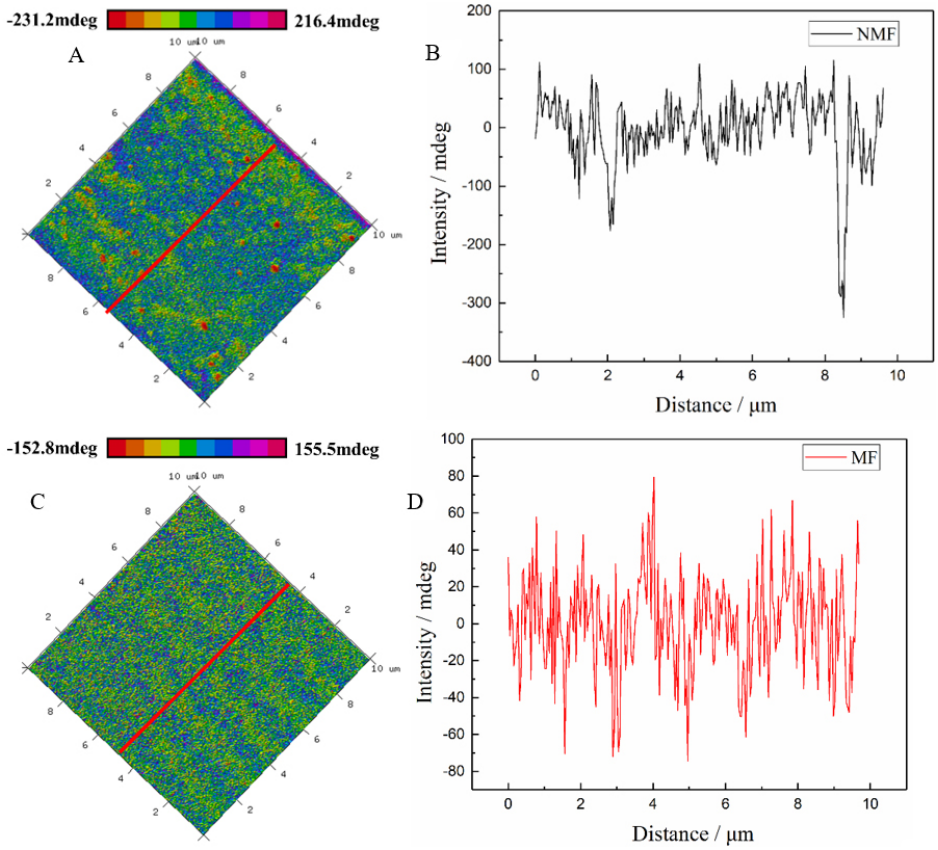

Figure 4. Magnetic domain distribution results of four coatings: (A) NMF 3D topography results; (B) NMF 2D topography results; (C) MF 3D topography results; (D) MF 2D topography results.

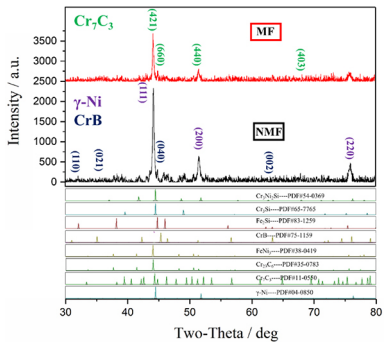

Figure 5. XRD test results of two coatings.

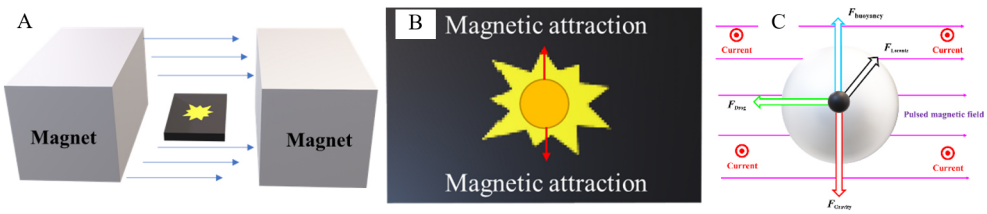

Figure 6. Forming mechanism of spray coating assisted by transverse static magnetic field: (A) magnetic field-assisted spraying model; (B) droplet spreading model; (C) droplet force model.

attracted by the magnetic field and pulled to both ends, as shown in Figure 6B.

Simultaneously, the droplets mostly exist in the molten or semi-molten state during the impact process and they capture the bubbles on the surface and form pores. However, because of the magnetic attraction, the solution flows. This gives bubbles more chance to escape the coating, which reduces the pores inside the coating. We then analyzed the force of stomatal movement in the static magnetic field, as shown in Figure 6C. The bubbles are subjected to gravity, buoyancy and drag forces exerted by the molten pool, resulting in a downward motion. The liquid drops cut the transverse static magnetic field in the coating molten pool, forming the direction of the induced current along the plane outward. The moving current will also be affected by the magnetic field to form the Lorentz force. The expression of F_{lorentz} force is as follows:

$$F_{\text{lorentz}} = \sigma \cdot (v2 \times B) \cdot B \quad (1)$$

where σ is the electrical conductivity, μ is the velocity of fluid flow and B is the magnetic induction intensity of the applied magnetic field. As shown by the blue arrow in Figure 6C, the direction of the Lorentz force is oblique upward. However, there is no metal solution inside the bubble and no induced current is generated around the molten pool. Thus, the Lorentz force is an interaction force that's downward sloping. Ultimately, the upward buoyancy of bubbles is affected, so the improvement of porosity is opposite to that shown in Figure 6B. However, because the coating forming process is the process of sudden cooling, its magnetic field strength is relatively small. The induced current will not be too large, so the bubble will still play a main role, as shown in Figure 6B. This reduces the porosity of the NMF coating. Simultaneously, the molten pool movement process is affected by the magnetic field, and there will be different phase transitions. The XRD phase structure of the coating changes, the hard phase increases and the performance of the coating will also be improved.

Mechanical properties of coatings

Residual stress of coatings

The residual stress tests of the two coatings are shown in Figure 7. The test results of residual stress were analyzed from the 0° and 90° directions. It can be seen from Figure 7 that the residual stress span of the MF sample is large, with stress distribution points from the first to the third quadrant. This indicates that the stress distribution of the MF sample is relatively random and less concentrated than that of NMF. Simultaneously, there are more negative residual stresses in MF than in NMF. This indicates that there is a significant residual compressive stress in the MF coating. Residual compressive stress can effectively alleviate the cracking and delamination failure of the coating. Therefore, it has a good effect on improving the service performance of the coating. The change of residual stress is related to the addition of magnetic field. When a transverse static magnetic field is applied, the impact of coating particles and the quenching process of forming coating particles will be affected by the magnetic field[23]. It can be seen from the phase change in Section "*Phase structure of coatings*" that the addition of magnetic field changes the phase result of the coating, which also leads to the change of residual stress of the coating[24,25].

Microhardness of coatings

The change in the cross-section hardness of the coating can reflect the change of the coating from the substrate to the surface of the coating, which is a good display of the coating hardness change trend. It can be seen from Figure 8 that the matrix hardness of the two samples is similar, but the hardness of the coating of the MF sample is generally higher than that of the NMF sample. The average hardness values of MF and NMF coatings are 638.46 and 785.45 MPa, respectively. This shows that the magnetic field can improve the

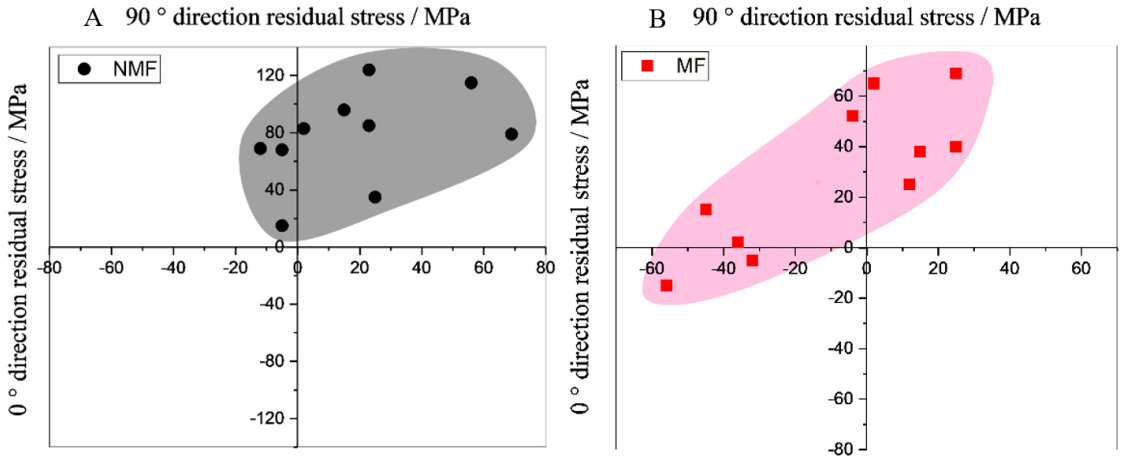

Figure 7. Residual stress distribution results of coatings: (A) NMF sample; (B) MF sample.

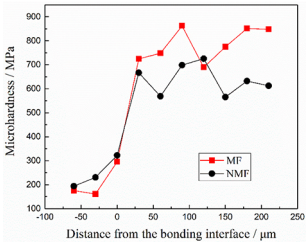

Figure 8. Microhardness test results of coatings.

performance of supersonic plasma spray coating. It can be seen from the XRD results that the addition of magnetic field increases the strengthening phase containing Cr in the coating. The presence of these phase structures directly increases the hardness of the coating. Simultaneously, the addition of the magnetic field reduces the pores in the cross section of the coating and the existence of pores will interfere with the measurement of hardness, resulting in a small hardness value. The combined effect of these two factors induces a good improvement in the hardness of the MF coating.

Tribological properties of coatings

The tribological curve of the coatings is shown in Figure 9. It can be seen that the two coatings fluctuate greatly at the beginning. However, with full contact between the friction pair and the coating, the Coefficient of friction (COF) orientation of the coating tends to be stable without excessive fluctuation. Comparing the COF curves of the two coatings, the mean values were 0.4220 and 0.4659, respectively. It can be found from the results that the COF of NMF coating is higher than that of MF coating. Simultaneously, we found that the middle of the COF curve of the NMF sample had an obvious onset. The main reason for the peak value of COF at this point is that large pores are encountered in the friction process, which will hinder the movement of the friction pair and increase the friction coefficient. However, as the pores are ground down, the COF value decreases again. Therefore, data fluctuations were formed, and the COF curve showed a peak. However, at the beginning of friction, the COF value of the MF sample decreases first and then gradually increases, which is related to the abrasive debris generated in the process of friction. With the progress of friction, there will be a large amount of abrasive debris, forming three-body wear and reducing the friction coefficient. With the development of friction process, the abrasive debris is taken away by the friction pair and the tribological curve rises gradually.

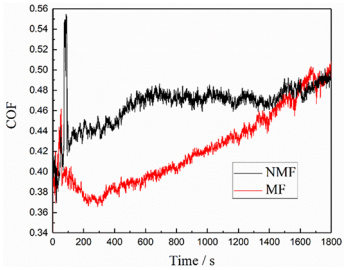

Figure 9. Tribological test results of the coatings.

Subsequently, we conducted a 3D morphological analysis on the wear marks of the coating, as shown in Figure 10. Figure 10A shows the results of the NMF sample and Figure 10C shows the results of the MF sample. The experimental friction parameters of the two coatings are the same. From the 2D numerical comparison of the two scratches, it can be found that the scratch depth in Figure 10B is deeper and the scratch length is longer than that in Figure 10D. Simultaneously, the wear volumes and rates of the two coatings were calculated, as shown in Table 2. The wear volumes of NMF and MF coatings were 0.196 and 0.183 × 10^{-3} mm^3, respectively, and their wear rates were 9.8 and 9.15, respectively, in units of (× 10^{-7}·mm^3/N·mm). According to the above results, under the same experimental conditions, the NMF coating has lower hardness and more pores, resulting in a larger wear volume of scratches and a higher wear rate.

Subsequently, the wear trace of the coatings was analyzed by SEM and EDS, as shown in Figure 11. From the macroscopic analysis of the wear trace morphology of the coatings, it is obvious that the NMF coating has more surface defects and is not as smooth as the MF coating. The furrow area on MF is also intact, which is related to the quality of the MF coating. After the magnetic field enhancement, the quality of the MF coating is improved and the wear morphology of the MF coating is consistent. The observation of the wear trace morphology of the two samples shows that NMFb is the accumulation of abrasive debris, and the friction pair pushes the abrasive debris to both sides through continuous reciprocating motion. This is basically consistent with the morphology of MFb. NMFc, d and e are spalling pits in the wear process. The existence of spalling pits will directly cause friction damage and friction coefficient fluctuation. In NMFd, the behavior of hierarchical failure also appears. NMFf is the oxidation failure morphology of the coating, and high strength O element can be seen from the energy spectrum, indicating that there is obvious oxidation failure here. On the contrary, the oxidation failure morphology of MFc shows that the oxidation area is smaller. NMFg is the abrasive debris stored in the spalling pit, which is collected by the spalling pit, and will reduce the effect of three-body wear. The wear morphology of the MF sample is basically consistent with that of NMF. We pay more attention to whether the MF sample will have better performance in the same wear pattern. From Figure MFd, it can be seen that the wear marks are smooth and the failure behavior is less during the surface friction process. MFe, Figure 11f and g are typical exfoliation pits and unexfoliated delamination failure locations. These positions are smaller than the size of the NMF sample, which can well prove that the quality of MF coating is relatively good and can exhibit better tribological properties.

CONCLUSIONS

In this study, a new Ni-based coating was prepared by transverse static magnetic field auxiliary equipment. The porosity of the coating decreased to less than 2%, and the residual compressive stress and microhardness increased. Furthermore, the tribological properties were also improved. This was related to the forming process of the coating under the transverse static magnetic field. Under the action of the

Table 2. Statistical results for tribological test parameters

	NMF	MF
Wear volume ($\times 10^{-3}$ mm^3)	0.196	0.183
Loading force (N)	40	40
Reciprocating distance (mm)	5	5
Wear rate ($\times 10^{-7}$·mm^3/N·mm)	9.8	9.15

NMF: Non-magnetic field; MF: magnetic field.

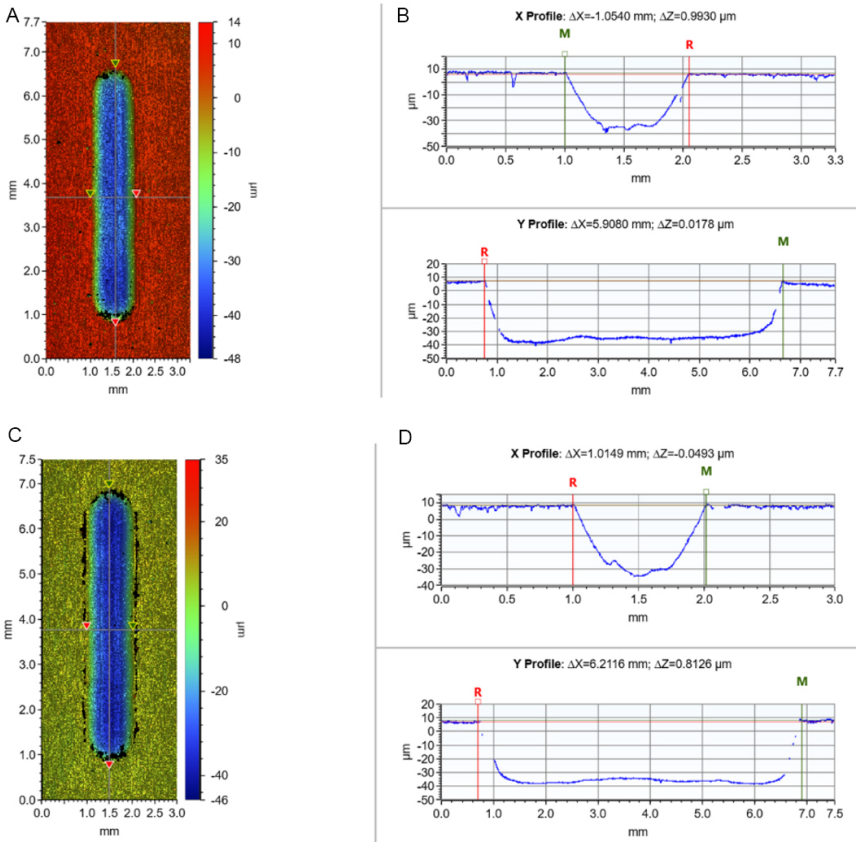

Figure 10. 3D morphologies of coating wear marks: (A) NMF 3D topography results; (B) NMF 2D topography results; (C) MF 3D topography results; (D) MF 2D topography results.

transverse static magnetic field, the powder showed magnetism and was attracted by the static magnetic field. Simultaneously, the solution in the molten pool was affected by the Lorentz force, which then affected the forming process of the coating. More hard phases containing Cr appeared in the coating and the magnetic domain distribution became more uniform. The service performance of the coating was improved by these effects.

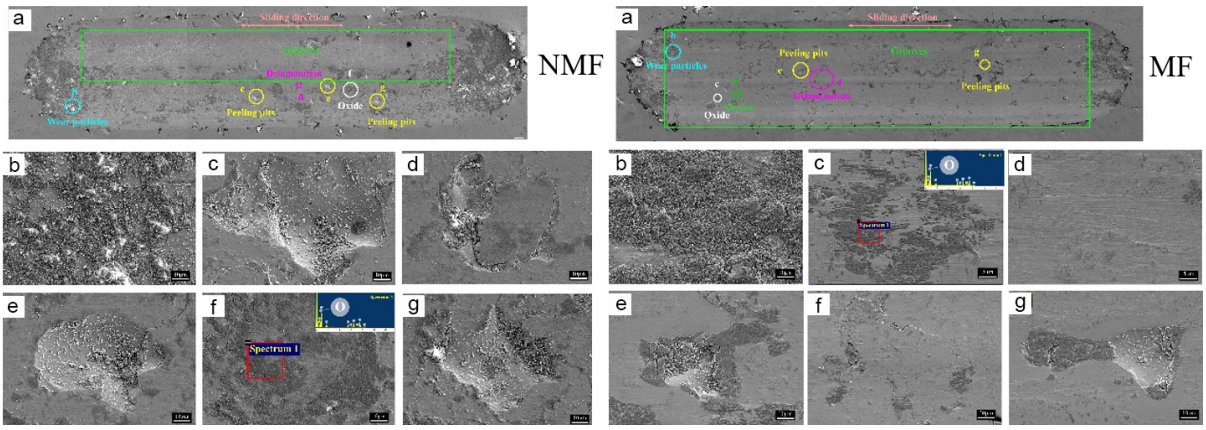

Figure 11. Wear morphology of NMF and MF coatings. (a) Overall morphology of wear marks. (b-g) High-multiple morphology of wear marks.

DECLARATIONS

Author's contributions

Conceptualization: Wang Z, Xing Z
Formal analysis: Wang Z
Methodology: Wang H
Data curation: Wang Z
Writing - original draft: Wang Z
Writing - review & editing: Huang Y
Supervision: Shan D

Availability of data and materials

Not applicable.

Financial support and sponsorship

The paper was financially supported by the General program of the National Natural Science Foundation of China (Grant No. 52130509) and Key basic research project of the Foundation Strengthening Plan (Grant No. 2019-JCJQ-JJ-034, 2019-JCJQ-ZD-302). The authors gratefully acknowledge the National Key Laboratory for Remanufacturing and Harbin Institute of Technology for supporting all the experiments. In addition, the authors would like to thank Huazhong University of Science and Technology for the debugging and repair of magnetic field equipment.

Conflicts of interest

The authors declare that they have no known competing financial interests or personal relationships that could have appeared to influence the work reported in this paper.

Ethical approval and consent to participate

Not applicable.

Consent for publication

Not applicable.

REFERENCES

1. Tan K, Wen X, Deng Q, Shen S, Liu L, Sharma P. Soft rubber as a magnetoelectric material - generating electricity from the remote action of a magnetic field. *Mater Today* 2021;43:8-16. DOI
2. Zhou D, Huang X, Ming Y, Li X, Li H, Li W. Material removal characteristics of magnetic-field enhanced shear thickening polishing technology. *J Mater Res Technol* 2021;15:2697-710. DOI
3. Tian Y, Luo W, Wang Y, et al. Ultrasound-assisted fast encapsulation of metal microparticles in SiO_2 via an interface-confined sol-gel method. *Ultrason Sonochem* 2021;73:105484. DOI PubMed PMC
4. Li A, Zhu Z, Liu Y, Hu J. Ultrasound-assisted electrodeposition of Fe-Ni film for OLED mask. *Mater Res Bull* 2020;127:110845. DOI
5. Pujar P, Madaravalli Jagadeeshkumar KK, Naqi M, et al. High-intensity ultrasound-assisted low-temperature formulation of lanthanum zirconium oxide nanodispersion for thin-film transistors. *ACS Appl Mater Interfaces* 2020;12:44926-33. DOI PubMed
6. Wang L, Wu C, Chen J, Gao J. Influence of the external magnetic field on fluid flow, temperature profile and humping bead in high speed gas metal arc welding. *Intern J Heat Mass Transfer* 2018;116:1282-91. DOI
7. Sitnikov BV, Marshuba VP. The influence of the welding circuit magnetic field on the formation of the joint at unsupported welding. *Weld Intern* 2019;33:399-404. DOI
8. Xiao Y, Liu T, Lu Z, et al. Instrument to characterize the wetting behavior of molten metal on a solid substrate under high magnetic field. *Rev Sci Instrum* 2019;90:063902. DOI PubMed
9. Zhang J, Chen F, Wang R, Qiao X, Chen H, Zhang X. Vector magnetic field measurement based on magnetic fluid and high-order cladding-mode Bragg grating. *Opt Laser Technol* 2021;143:107264. DOI
10. Wang Q, Zhai LL, Zhang L, Zhang JW, Ban CY. Effect of steady magnetic field on microstructure and properties of laser cladding Ni-based alloy coating. *J Mater Res Technol* 2022;17:2145-57. DOI
11. Yin N, Xing Z, He K, Zhang Z. Tribo-informatics approaches in tribology research: a review. *Friction* 2022. DOI
12. Pan S, Jin K, Wang T, Zhang Z, Zheng L, Umehara N. Metal matrix nanocomposites in tribology: manufacturing, performance, and mechanisms. *Friction* 2022. DOI
13. Qi K, Yang Y, Sun R, et al. Effect of magnetic field on crack control of Co-based alloy laser cladding. *Opt Laser Technol* 2021;141:107129. DOI
14. Tharajak J, Palathai T, Sombatsompop N. The effects of magnetic field-enhanced thermal spraying on the friction and wear characteristics of poly(ether-ether-ketone) coatings. *Wear* 2017;372-373:68-75. DOI
15. Hu G, Yang Y, Sun R, Qi K, Lu X, Li J. Microstructure and properties of laser cladding NiCrBSi coating assisted by electromagnetic-ultrasonic compound field. *Surf Coat Technol* 2020;404:126469. DOI
16. Tan N, Li Y, Lou L, Zhang G, Xing Z, Wang H. Influence of micro-nano multiscale surface texture on wettability of Ni-based droplets at high temperature. *Surf Coat Technol* 2021;418:127103. DOI
17. He P, Wang H, Chen S, et al. Interface characterization and scratch resistance of plasma sprayed TiO2-CNTs nanocomposite coating. *J Alloys Compd* 2020;819:153009. DOI
18. Tang L, Kang J, He P, et al. Effects of spraying conditions on the microstructure and properties of NiCrBSi coatings prepared by internal rotating plasma spraying. *Surf Coat Technol* 2019;374:625-33. DOI
19. Wang Z, Huang Y, Zhou J, et al. Effect of Fe content on the tribological properties of Ni60 coatings applied by pulsed magnetic field assisted supersonic plasma spraying. *Mater Charact* 2022;185:111771. DOI
20. Hua S, De Graef M. Comparison of magnetic domain wall images using lorentz microscopy and magnetic force microscopy. *Microsc Microanal* 2013;19:790-1. DOI
21. Cullity BD, Graham CD. Introduction to magnetic materials[M] John Wiley & Sons. 2008. DOI
22. Donaldson L. New storage platforms from spin ice. *Mater Today* 2012;15:187. DOI
23. Skalka P, Slámečka K, Pokluda J, Čelko L. Finite element simulation of stresses in a plasma-sprayed thermal barrier coating with a crack at the TGO/bond-coat interface. *Surf Coat Technol* 2018;337:321-34. DOI
24. Nayebpashaee N, Seyedein S, Aboutalebi M, Sarpoolaky H, Hadavi S. Finite element simulation of residual stress and failure mechanism in plasma sprayed thermal barrier coatings using actual microstructure as the representative volume. *Surf Coat Technol* 2016;291:103-14. DOI
25. Kamara A, Davey K. A numerical and experimental investigation into residual stress in thermally sprayed coatings. *Intern J Solids Struct* 2007;44:8532-55. DOI